Correcting chromatic offset in multicolor super-resolution localization microscopy

Miklos Erdelyi,[1,2,3,*] Eric Rees,[1] Daniel Metcalf,[2] Gabriele S. Kaminski Schierle,[1] Laszlo Dudas,[3] Jozsef Sinko,[3] Alex E. Knight,[2] and Clemens F. Kaminski[1,4]

[1]*Department of Chemical Engineering and Biotechnology, University of Cambridge, Pembroke Street, Cambridge, CB2 3RA, UK*

[2]*Analytical Science Division, National Physical Laboratory, Hampton Road, Teddington, TW11 0LW, UK*

[3]*Department of Optics and Quantum Electronics, University of Szeged, Szeged, Dómtér9 6720, Hungary*

[4]*cfk23@cam.ac.uk*

**meerdelyi@gmail.com*

Abstract: Localization based super-resolution microscopy techniques require precise drift correction methods because the achieved spatial resolution is close to both the mechanical and optical performance limits of modern light microscopes. Multi-color imaging methods require corrections in addition to those dealing with drift due to the static, but spatially-dependent, chromatic offset between images. We present computer simulations to quantify this effect, which is primarily caused by the high-NA objectives used in super-resolution microscopy. Although the chromatic offset in well corrected systems is only a fraction of an optical wavelength in magnitude (<50 nm) and thus negligible in traditional diffraction limited imaging, we show that object colocalization by multi-color super-resolution methods is impossible without appropriate image correction. The simulated data are in excellent agreement with experiments using fluorescent beads excited and localized at multiple wavelengths. Finally we present a rigorous and practical calibration protocol to correct for chromatic optical offset, and demonstrate its efficacy for the imaging of transferrin receptor protein colocalization in HeLa cells using two-color direct stochastic optical reconstruction microscopy (*d*STORM).

OCIS codes: (180.2520) Fluorescence microscopy; (100.6640) Superresolution.

References and links

1. M. Born and E. Wolf, *Principles of Optics* (Cambridge University Press, 2002)
2. S. W. Hell, "Far-field optical nanoscopy," Science **316**(5828), 1153–1158 (2007).
3. E. Betzig, G. H. Patterson, R. Sougrat, O. W. Lindwasser, S. Olenych, J. S. Bonifacino, M. W. Davidson, J. Lippincott-Schwartz, and H. F. Hess, "Imaging intracellular fluorescent proteins at nanometer resolution," Science **313**(5793), 1642–1645 (2006).
4. S. T. Hess, T. P. K. Girirajan, and M. D. Mason, "Ultra-high resolution imaging by fluorescence photoactivation localization microscopy," Biophys. J. **91**(11), 4258–4272 (2006).
5. M. J. Rust, M. Bates, and X. Zhuang, "Sub-diffraction-limit imaging by stochastic optical reconstruction microscopy (STORM)," Nat. Methods **3**(10), 793–796 (2006).
6. M. Heilemann, S. van de Linde, A. Mukherjee, and M. Sauer, "Super-resolution imaging with small organic fluorophores," Angew. Chem. Int. Ed. Engl. **48**(37), 6903–6908 (2009).
7. J. Fölling, M. Bossi, H. Bock, R. Medda, C. A. Wurm, B. Hein, S. Jakobs, C. Eggeling, and S. W. Hell, "Fluorescence nanoscopy by ground-state depletion and single-molecule return," Nat. Methods **5**(11), 943–945 (2008).
8. R. E. Thompson, D. R. Larson, and W. W. Webb, "Precise nanometer localization analysis for individual fluorescent probes," Biophys. J. **82**(5), 2775–2783 (2002).
9. E. J. Rees, M. Erdelyi, D. Pinotsi, A. Knight, D. Metcalf, and C. F. Kaminski, "Blind assessment of localization microscopy image resolution," Opt. Nanoscopy **1**(1), 12 (2012).
10. S. H. Lee, M. Baday, M. Tjioe, P. D. Simonson, R. Zhang, E. Cai, and P. R. Selvin, "Using fixed fiduciary markers for stage drift correction," Opt. Express **20**(11), 12177–12183 (2012).

#185209 - $15.00 USD Received 11 Feb 2013; revised 8 Apr 2013; accepted 18 Apr 2013; published 26 Apr 2013

11. M. J. Mlodzianoski, J. M. Schreiner, S. P. Callahan, K. Smolková, A. Dlasková, J. Santorová, P. Ježek, and J. Bewersdorf, "Sample drift correction in 3D fluorescence photoactivation localization microscopy," Opt. Express **19**(16), 15009–15019 (2011).
12. S. Stallinga and B. Rieger, "Accuracy of the Gaussian point spread function model in 2D localization microscopy," Opt. Express **18**(24), 24461–24476 (2010).
13. H. Bock, C. Geisler, C. A. Wurm, C. von Middendorff, S. Jacobs, A. Schonle, A. Egner, S. W. Hell, and C. Eggeling, "Two-color far-field fluorescence nanoscopy based on photoswitchable emitters," Appl. Phys. B **88**(2), 161–165 (2007).
14. S. van de Linde, U. Endesfelder, A. Mukherjee, M. Schüttpelz, G. Wiebusch, S. Wolter, M. Heilemann, and M. Sauer, "Multicolor photoswitching microscopy for subdiffraction-resolution fluorescence imaging," Photochem. Photobiol. Sci. **8**(4), 465–469 (2009).
15. L. S. Churchman and J. A. Spudich, "Colocalization of fluorescent probes: accurate and precise registration with nanometer resolution," in *Single-Molecule Techniques: A Laboratory Manual*. P. R. Selvin, and T. Ha eds. (Cold Spring Harbor Laboratory Press, 2008), pp. 73–84.
16. M. Bates, G. T. Dempsey, K. H. Chen, and X. Zhuang, "Multicolor super-resolution fluorescence imaging via multi-parameter fluorophore detection," ChemPhysChem **13**(1), 99–107 (2012).
17. I. Testa, C. A. Wurm, R. Medda, E. Rothermel, C. von Middendorf, J. Fölling, S. Jakobs, A. Schönle, S. W. Hell, and C. Eggeling, "Multicolor fluorescence nanoscopy in fixed and living cells by exciting conventional fluorophores with a single wavelength," Biophys. J. **99**(8), 2686–2694 (2010).
18. D. Baddeley, D. Crossman, S. Rossberger, J. E. Cheyne, J. M. Montgomery, I. D. Jayasinghe, C. Cremer, M. B. Cannell, and C. Soeller, "4D super-resolution microscopy with conventional fluorophores and single wavelength excitation in optically thick cells and tissues," PLoS ONE **6**(5), e20645 (2011).
19. A. Pertsinidis, Y. Zhang, and S. Chu, "Subnanometre single-molecule localization, registration and distance measurements," Nature **466**(7306), 647–651 (2010).
20. A. Löschberger, S. van de Linde, M. C. Dabauvalle, B. Rieger, M. Heilemann, G. Krohne, and M. Sauer, "Super-resolution imaging visualizes the eightfold symmetry of gp210 proteins around the nuclear pore complex and resolves the central channel with nanometer resolution," J. Cell Sci. **125**(3), 570–575 (2012).
21. Y. Fujimoto and T. Kasahara, "Immersion objective lens system for microscope", US patent US 7,199,938 B2 (2007).
22. Lambda Research Corp., *OSLO optics software, optics reference* ver. 6.1.
23. M. Mandai and K. Yamaguchi, "Immersion microscope objective lens", US patent US 7,046,451 B2 (2006).
24. http://laser.cheng.cam.ac.uk/wiki/index.php/Resources
25. M. Ahn, E. De Genst, G. S. Kaminski Schierle, M. Erdelyi, C. F. Kaminski, C. M. Dobson, and J. R. Kumita, "Analysis of the native structure, stability and aggregation of biotinylated human lysozyme," PLoS ONE **7**(11), e50192 (2012).
26. G. S. Kaminski Schierle, S. van de Linde, M. Erdelyi, E. K. Esbjörner, T. Klein, E. Rees, C. W. Bertoncini, C. M. Dobson, M. Sauer, and C. F. Kaminski, "In situ measurements of the formation and morphology of intracellular β-Amyloid fibrils by super-resolution fluorescence imaging," J. Am. Chem. Soc. **133**(33), 12902–12905 (2011).
27. G. T. Dempsey, J. C. Vaughan, K. H. Chen, M. Bates, and X. Zhuang, "Evaluation of fluorophores for optimal performance in localization-based super-resolution imaging," Nat. Methods **8**(12), 1027–1036 (2011).

1. Introduction

In traditional fluorescence microscopy the signals from molecules whose separation is less than the Rayleigh diffraction limit [1] cannot be distinguished because their point spread functions (PSF) overlap in the formed image, leading to image blur. The problem becomes pronounced when there are significant numbers of fluorophores in the sample situated at distances less than about an optical wavelength away from one another. The best possible spatial resolution achievable with conventional microscopy techniques is thus around half the wavelength of light.

Several methods have been developed to overcome this diffraction limitation, collectively referred to as optical super-resolution imaging techniques [2]. The present paper is concerned with a class of super-resolution techniques called localization microscopy, which include PALM, STORM, dSTORM and GSDIM [3–7]. The principle behind all of these techniques is that images are recorded from spatially sparse fluorophore subsets of densely labeled samples so that individual PSFs do not overlap in the recorded images. The position of individual molecules can then be inferred from the center position of individual PSFs via computational fitting routines with a precision much better than that dictated by the Rayleigh diffraction limit [8, 9]. Theoretically this precision is limited only by the number of photons recorded from each emitter. In practice, resolution is affected by several error sources and the

#185209 - $15.00 USD Received 11 Feb 2013; revised 8 Apr 2013; accepted 18 Apr 2013; published 26 Apr 2013

localization precision which is routinely achievable in most laboratories lies in the 10 to 20 nm range.

Motion artifacts constitute one major source of such errors. In a typical experiment several thousand image frames are acquired over time scales of a few minutes, and sample or mechanical movements must be carefully controlled, a subject of numerous publications in the field [10, 11]. Another source of systematic error, much less often discussed in the literature, stems from imperfections in the optical imaging system, which can lead to asymmetries and co-ordinate dependent variations of the microscope's optical transfer function (OTF) [12]. Even the most highly corrected lens systems exhibit imperfections on the sub-20 nm scale. In single-color localization microscopy experiments the latter effects are usually ignored as they do not *per se* affect the localization precision for individual molecules, but rather cause image distortion. However, in multicolor experiments this is no longer true, because usually there is a chromatic dependence of these distortions, and this negatively affects one's ability to co-localize fluorophores of different colors. Yet the capability of co-localizing two (or more) colors is essential to address many biological questions (e.g. "Are two proteins associated within the same subcellular domain?"), and the number of multicolor super-resolution applications is steadily rising. In previous work, optical offsets in the 50-150nm range have been reported in such applications between different color channels [13, 14].

Two approaches to multi-color imaging can be distinguished. The sequential approach captures the two (or more) images at different times and uses the full size of the CCD chip. This approach (i) uses the full size of the CCD chip, and therefore has a larger FOV; (ii) introduces minimum loss of light because of the reduced number of optical components in the emission pathway; (iii) minimizes optical aberrations because all the optical elements can be centered, (iv) introduces minimal cross-talk between the two channels; and (v) increases the time of measurement because of the sequential data acquisition. In the simultaneous approaches, the image is split into two spectral channels and then imaged onto different regions of the CCD chip [15]. This method (i) typically introduces more optical aberration because of the additional (and imperfectly centered) optical components; (ii) reduces the localization precision because of the higher loss of light; (iii) reduces the FOV; (iv) speeds up the measurement because of the simultaneous acquisition of the two spectral channels. In our work we favor the sequential method and this is the focus of the work described in this paper.

In practice, fiducial markers, such as gold nanoparticles, can be introduced into the sample to provide reference coordinates in each of the color channels [16–18].These then permit co-registration algorithms to be applied in a post processing step to map image co-ordinates from the different color channels onto one another. Co-localization precisions of the order of a few nanometers have been reported with this approach [19]. The introduction of fiducial markers is often impractical, however, especially in biological samples. A different approach uses information directly from the sample itself to co-register different color image channels, but this is successful only in a few special cases [20] and also requires an *a priori* knowledge about the sample that is not usually available. It is therefore timely to explore in depth the problem of chromatic aberration in multicolor localization microscopy, and this is the subject of the present paper. We provide both experimental and theoretical results to assess effects of chromatic aberrations and present strategies for optimal performance in practical imaging situations.

2. Computer simulations

For the accurate registration of multicolor super-resolved images it is essential to distinguish between the effects of mechanical drift and optical offset. Mechanical drift is a time-dependent but a spectrally and spatially invariant process, i.e. it can be described by a function $\boldsymbol{r}_{drift}(t)$. In contrast, optical offset is independent of time, but has a positional dependence $\boldsymbol{r}_{offset}(x,y)$ across the image plane. Therefore, the total displacement $\boldsymbol{r}_{tot}(x,y,t)$ =

#185209 - $15.00 USD Received 11 Feb 2013; revised 8 Apr 2013; accepted 18 Apr 2013; published 26 Apr 2013

$\boldsymbol{r}_{drift}(t)$ + $\boldsymbol{r}_{offset}(x,y)$ has both spatial and temporal dependence. In single-color localization microscopy the optical offset term is not taken into consideration, because the exact (aberration free) image is unknown, and sub-wavelength distortions typically do not affect the interpretation of the final super-resolved images. However, the offset term is also wavelength dependent. For example in two-color experiments, which we consider here, the differential offset (optical chromatic offset) between the two different wavelengths becomes $\Delta\boldsymbol{r}_{offset}(x,y,\lambda_{1,2}) = \boldsymbol{r}_{offset}(x,y,\lambda_1)-\boldsymbol{r}_{offset}(x,y,\lambda_2)$, which can be larger than the pixel size in the super-resolved image and thus lead to errors and misinterpretation of image information.

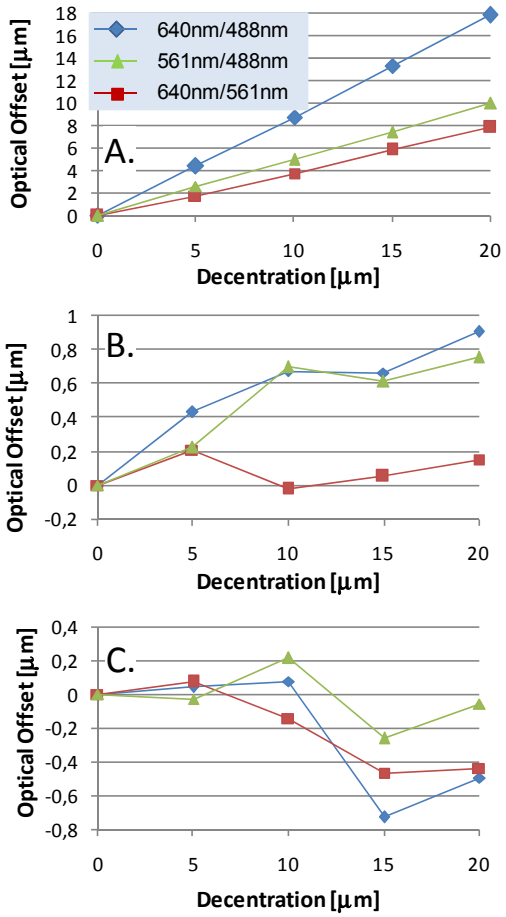

Fig. 1. Calculated optical offset as a function of decentration of a point-like source at three different excitation wavelength pairs and under three different optical conditions: microscope objective only (A), tilted dichroic mirror (B) and wedged emission filter (C).

In practice, fiducial markers (fluorescent beads, gold nano-particles, etc.) emitting in the same wavelength range as the applied dyes are typically used for drift correction and image registration. However, in this case the separation of the position dependent optical-offset from the mechanical drift is a challenge. The density of the applied markers in the field-of-view (FOV) is typically low (ideally only one in the FOV), hence the spatial dependence of the displacement cannot be determined. Increasing the number of markers in the FOV makes possible the determination of optical offset but reduces the effective FOV since structures in the close vicinity of the bright markers cannot be imaged. Separation of drift correction from super-resolution imaging (e.g. using beads with different excitation and emission wavelengths to the sample) can address this issue. In this case the mechanical drift can be measured

#185209 - $15.00 USD Received 11 Feb 2013; revised 8 Apr 2013; accepted 18 Apr 2013; published 26 Apr 2013

separately, and the captured frames can be registered and corrected for the optical offset independently. Assuming that microscope coverslips are identical, and the imaged region of interest (ROI) is close to the surface (as with TIRF or highly inclined illumination), the optical offset is a static displacement, introduced by the optical components, and can be measured in advance during a calibration procedure.

Here we investigate the origin of optical offsets and present a method for their mitigation. Both experimental measurements and ray-tracing calculations are presented. For calculations we assumed the fluorophore emission to be independent of excitation conditions (illumination angle and polarization), and the fluorescent dye molecules were assumed to be point-like sources emitting unpolarized light. The microscope objective was modeled as an apochromat immersion lens system with magnification, numerical aperture and focal length of 100 × , 1.41 and 1.8 mm, respectively [21]. The tube lens was modeled as a perfect lens with a focal length of 180mm. The dichroic mirror and the emission filter were modeled as1.1 mm and 3.5 mm thin silica (n = 1.4584, V = 67.82) plates inserted between the microscope objective and the tube lens. The polychromatic point spread function was calculated using the direct integration method [22] with a spatial resolution of 0.78 μm in an evaluation window of 0.2mm × 0.2mm. The center position of the evaluation window roughly equals the geometrical image of the point-like source (decentration of the light source × magnification). The off-axis position of the PSF was determined as the sum of the center position of the evaluation window and the peak position of the PSF relative to the center of the evaluation window. Three spectral ranges were selected corresponding to the transmission windows of the dichroic and emission filter sets used (Di01-R405/488/561/635-25x36 and FF01-446/523/600/677-25, both from Semrock). The three wavelengths used for calculation of polychromatic PSF in OSLO [22]for the three transmission windows are listed in Table 1.

Table 1. Excitation and emission wavelengths used for experiments and simulations

Excitation wavelengths	Transmission windows of the emission filter (T_{avg}>90%)	Applied wavelengths for polychromatic imaging in OSLO		
		λ_1	λ_2	λ_2
491 nm	502 nm – 544 nm	523 nm	502 nm	544 nm
561 nm	582 nm – 617 nm	600 nm	582 nm	617 nm
640 nm	663 nm – 690 nm	676 nm	663 nm	690 nm

The off-axis position of the calculated PSF as a function of decentration (marked as DCY in OSLO) of the point-like light source was calculated for the three transmission windows. In the following the appropriate excitation wavelengths will be used as references for the three excitation/emission spectral windows. The optical offsets – defined as the spatial shift of the peak positions at different excitation wavelength pair combinations– are depicted in Fig. 1 (blue: 640nm/491nm; green: 561nm/491nm; red: 640nm/561nm).

Without additional filters in the optical path the offset was found to be a linear function of the decentration of the point-like source (Fig. 1(A)) with a value of 8-10 μm at the edge of the plotted FOV(40 × 40 μm). In this case, only cylindrically symmetric aberrations were introduced by the microscope objective. Figure 1(B) and 1(C) depict the net optical offset introduced by a tilted dichroic (45°) and a wedged (0.08°) emission filter. The tilted surfaces introduced asymmetric aberrations such as coma and astigmatism. The maximum values of the optical offset measured as a function of the tilt and the wedge were found to be insignificant, almost one order of magnitude smaller than the error introduced by the objective. In other words, the computer simulations show that the main source of optical aberrations is the microscope objective itself. The simulations predict a position-dependent optical offset: the larger the decentration of the multi-labeled point-like source, the larger the optical offset. We have repeated the simulations using a high NA Nikon objectives [23] with almost identical results. We believe the optimization criteria for such objectives are similar: the lateral chromatic aberration should be smaller than the diffraction limit (typically equal to

#185209 - $15.00 USD Received 11 Feb 2013; revised 8 Apr 2013; accepted 18 Apr 2013; published 26 Apr 2013

the pixel size of the CCD camera in localization techniques). Therefore, we do not expect serious differences between TIRF objectives from different manufacturers and think that the simulation results described above are typical values can be used in general.

3. Experimental details

A schematic representation of the experimental system used is shown in Fig. 2. Experiments were performed on an inverted microscope frame (Nikon TE300), which was used in a custom-built dSTORM system [24] as shown in Fig. 2. The beams of four lasers operating at 405 nm (Mitsubishi Electric Corp. ML320G2-11), 491 nm (Cobolt Calypso), 561 nm (Oxxius SLIM-561) and 640 nm (Toptica, iBeam smart), were co-aligned and collimated using dichroic mirrors and a beam expanding telescope (achromatic lenses: L_1 and L_2in Fig. 2). The light beam was directed into the microscope frame by means of two periscope mirrors (M_1 and M_2) and focused into the back focal plane of the objective (O: Nikon TIRF NA: 1.49, M: 100 ×) *via* an achromatic focusing lens (L_3). Mirror M_2 was placed into the front focal plane of focusing lens L_3. This permits convenient control of illumination conditions and continuous variation between EPI, HI (highly inclined), and TIRF illumination modes, which is achieved simply by tilting mirror M_2.A multi-edge filter set (BrightLineLF405/488/561/635-A-000,Semrock) was installed, permitting sample excitation and fluorescence detection at multiple wavelength combinations. A 1 × telescope (achromatic lenses: L_4 and L_5) was installed in front of the detector (EMCCD DU-897E, Andor, camera pixel size: 16 µm). The 16 µm physical CCD pixel size corresponds to 160 nm pixel size on a traditional image due to the 100 × magnification of the objective. The typical improvement in resolution of our STORM microscope is a factor of 10, therefore the super-resolution images are reconstructed with a corresponding 16 nm pixel width, throughout this paper.

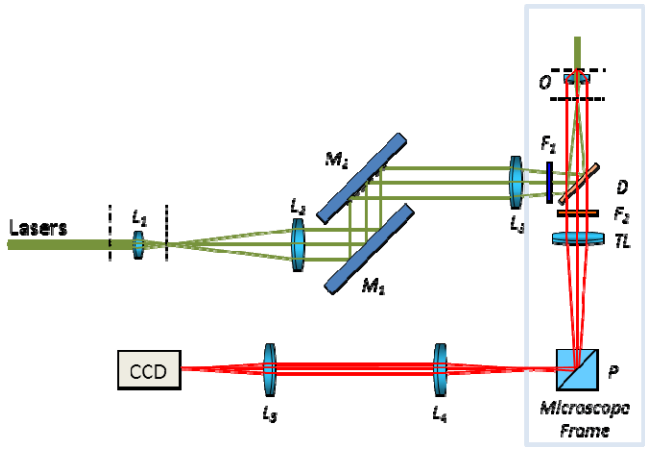

Fig. 2. Schematic view of the optical setup. Laser beams were expanded by lenses L_1 (Thorlabs, AC127-025-A) and L_2 (Thorlabs, AC254-150-A) and focused into the back focal plane of the microscope objective (O) by means of lens L_3 (Thorlabs, AC508-250-A). Dotted and dashed lines depict the conjugate planes of the system. The image generated by the objective and tube lens (TL) was imaged into a CCD camera via a 1 × telescope formed by lenses L_4 and L_5 (Thorlabs, AC254-100-A). Multi-edge excitation (F_1) and emission filters (F_2) and a dichroic mirror (D) were applied to spectrally separate the excitation and emission light. The illumination condition was set via mirror M_2 placed into the front focal plane of the focusing lens L_3.

As test samples we used multicolored fluorescence beads of 100 nm diameter (Invitrogen Molecular Probes, T7279) adhering to a coverslip (Thermo Fisher Scientific, Lab-Tek chamber, 155411). The surface density of beads was sufficiently low to permit the localization of individual beads.

#185209 - $15.00 USD Received 11 Feb 2013; revised 8 Apr 2013; accepted 18 Apr 2013; published 26 Apr 2013

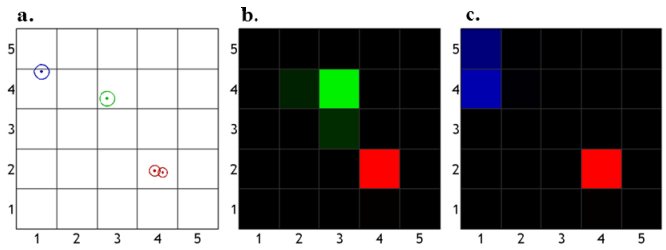

Fig. 3. Localization of a single fluorescent bead upon sequential excitation at 640(R), 561(G), 488(B) and 640 nm, respectively. a: Localization positions (dots) and errors (circles) for all the wavelengths calculated from the200-frame sub-stacks. Colocalized STORM images of R/G (b) and R/B (c) excitation pairs. The super-resolved pixel size is 16 nm by 16 nm.

For the measurements shown, image stacks with 800 frames were captured. The excitation wavelength was sequentially changed between 640, 561, 491 and 640 nm during acquisition so that 200 frames would be captured at every wavelength. The repeat localization at the end of the sequence at 640 nm was used to estimate mechanical drift during data acquisition. Figure 3(a) shows the optical offset based on sequential localization of a single multicolor fluorescent bead. The localization precision (as defined by Thompson [8]) was <3 nm for the 640 nm and <4 nm for the 488 nm and 561 nm excitations respectively, at an exposure time of 100 ms. The excellent 3-4 nm localization precision achieved with the bright fluorescent beads ensures that image registration can be applied to real localization microscopy data (with typical precision of 10-30 nm) without causing any significant loss of resolution [9]. The excellent co-localization between the first and the last sub-stacks proves (red circles in Fig. 3(a)) that mechanical drift did not significantly degrade the super-resolved image quality. However, localization of the same bead via excitation with the 561 nm and 488 nm lasers shows $\Delta \boldsymbol{r}_{offset}(\lambda_{640,561}) \approx 2$ and $\Delta \boldsymbol{r}_{offset}(\lambda_{640,488}) \approx 3$ super-resolved pixels, respectively. These optical offsets correspond to a displacement error of 30-45 nm, the diameter of many smaller vesicles in cells.

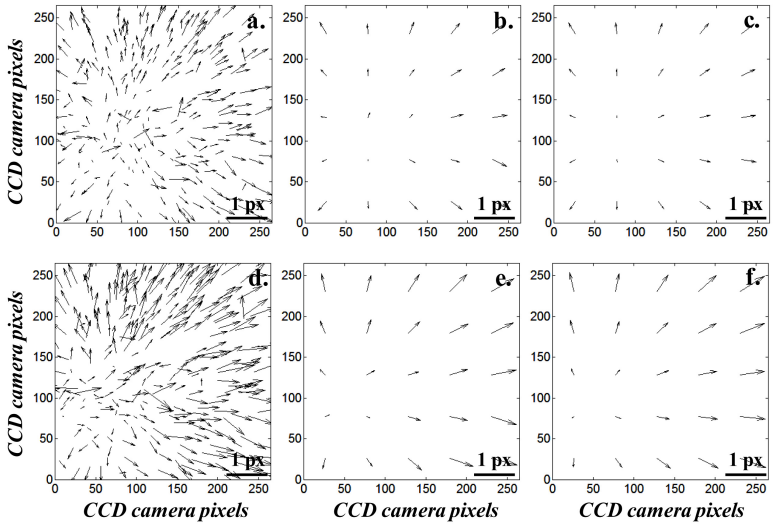

Fig. 4. Experimental determination of spatial dependence of optical offset using excitation wavelengths 641 nm/561 nm (a, b, c) and 641 nm/491 nm (d, e, f). Raw (a, d) and averaged (b, e) data of four sequentially captured frames. Polynomial fitting (c, f) to the measured data provides a smooth distribution and allows determination of optical offset at an arbitrary point. Vectors representing optical offset were magnified for easier visualization (axes represent spatial position in pixels, and scale bars represent optical offset, also in camera pixels).

#185209 - $15.00 USD Received 11 Feb 2013; revised 8 Apr 2013; accepted 18 Apr 2013; published 26 Apr 2013

The spatial variation of optical offset was determined over larger fields of view on the sample, (FOV = 41 μm × 41 μm) from multiple beads, and the corresponding data is shown in Fig. 4(a) and 4(d) for the 640 nm/561 nm and the 640 nm/491 nm excitation wavelength combinations, respectively. The variation of the optical offset shown exhibited a radially symmetric pattern, varying from 0 in the center to approximately 16 μm (1 camera pixel) values at the edge of the FOV measured on the camera, in good agreement with the ray tracing simulations. Some movement of individual beads was observed during data acquisition, an effect that can be mitigated by averaging. Figures 4(b) and 4(e) show the averaged values of optical offset in the 5 × 5 sub regions. The trend of optical offset can be seen clearly, although there are regions (for example: first column, fourth row in Fig. 4(e)) with aberrant values, probably because of a low density of localized beads in that region, or detachment of beads from the coverslip surface. Since optical offset is a static displacement, images captured and evaluated sequentially can be used to mitigate this undesirable effect. Alternatively, a polynomial can be fitted to the measured data (Figs. 4(a) and 4(d)) that results in a smooth spatial distribution of optical offset (Figs. 4(c) and 4(f)). We fitted the observed optical offset of the beads with a second order polynomial transform, using the MATLAB (cp2tform) library routine. We found that the second order polynomial provided a good fit to the measured optical offset, without overfitting. (This is demonstrated by the better fits observed in the offset-corrected bead positions.)This approach assumes that optical aberration, the mean source of optical offset is a slowly varying function of spatial coordinates. The fitted polynomial parameters can be used to determine optical offset in any spatial position inside the FOV.

4. Results and discussion

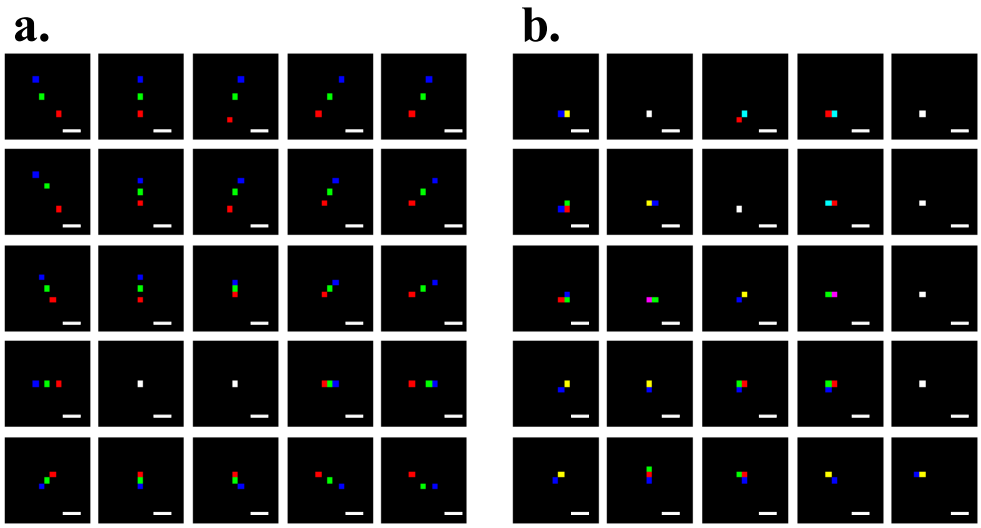

Fig. 5. Localization of a single multicolored bead from every sub-region using 488 nm (blue), 561 nm (green) and 640 nm (red) excitation before (a) and after (b) optical offset correction. Each tile corresponds to an area of 240 x 240 nm^2. Adjacent tiles are separated by 10 μm in the image plane, to provide representative samples across the entire FOV of 41 μm × 41 μm. Scale bars: 50nm.

The optical offset vector maps permit the calibration of optical super-resolution microscopes to correct for effects of chromatic offset. The calibration is dependent on the alignment of the optical imaging train in the microscope (microscope objective, filters, additional optics, etc.), and may require recalibration if the imaging system has been modified (i.e. changing the position of any optical components, such as the objective). Figure 5(a) shows images obtained

#185209 - $15.00 USD Received 11 Feb 2013; revised 8 Apr 2013; accepted 18 Apr 2013; published 26 Apr 2013

from single beads placed in representative sub-regions across the FOV using excitation wavelengths 491 nm (blue), 561 nm (green), and 640 nm (red). The same FOV (41 μm × 41 μm) was applied as before. Using the inbuilt image registration algorithm of MATLAB, the optical offset can be effectively reduced based on the previously captured vector maps (Figs. 4(c) and 4(f)) as shown in Fig. 5(b). After correction, the maximum colocalization error was of the order of one super-resolved pixel (16 nm on the sample), smaller than the tolerable error in multicolor localization based microscopy. However, using a smaller FOV (typically areas smaller than 20 μm × 20 μm are used in techniques such as STORM to ensure even illumination conditions) the co-localization error is even smaller than what is reported here.

The MATLAB software we developed for localization microscopy is available on the World Wide Web [24]. This set of MATLAB routines performs localization on raw data and visualization of fluorophore density, as well as post-processing to remove translational drift (via fiducial markers), and so it can calibrate and correct for optical offset as described in this paper.

We applied the technique to a representative biological problem, namely the clustering of cell surface proteins which mediates endocytosis. In particular, we investigated the clustering of transferrin protein upon binding to cell membrane receptors and the subsequent formation of vesicular structures. For this purpose we conjugated batches of transferrin protein to either Alexa 568 (green) or Alexa 647 (red) dyes, and subsequently incubated HeLa cells at 37°C for 10 minutes with mixtures containing both conjugates in equal measure. The transferrin molecules were thus allowed to bind to their receptors at the cell surface, resulting in receptor stimulation and clustering into cell surface vesicles which become endocytosed (internalized) and transported into endosomes.

We used the setup as shown in Fig. 2 to perform both diffraction-limited TIRF and direct stochastic optical reconstruction microscopy (*d*STORM) super-resolution imaging on the cells. The details for *d*STORM follow our earlier reports [9, 25, 26]. Two-color *d*STORM images were captured sequentially, first in the red (Alexa 647) and then in the green image channels (Alexa 568) at excitation wavelengths of 640 and 561 nm, respectively. Switching buffers containing oxygen scavenger and β-mercaptoethylamine (MEA) were used for *d*STORM imaging as reported in [26]. Image stacks of 10,000 frames were collected at frame exposure times of 20 ms.

Figure 6 shows the results of the two-color diffraction-limited TIRF and super-resolved *d*STORM imaging. Diffraction-limited TIRF images showed, as expected, that the transferrin proteins conjugated to the different dyes adhere to cells at similar concentrations (Figs. 6(a) and 6(b)). However, TIRF images could not reveal their clustering and condensation into vesicular structures; in contrast, the latter are clearly resolved in the *d*STORM images (Figs. 6(c) and 6(d)). The images for the two color channels appear slightly different (Figs. 6(c) and 6(d)), which reflects a combination of the different switching performances of the two dyes (Alexa 647 is more efficient for *d*STORM imaging), and local concentration variations of the two labeled species across the cell surface [27]. Figure 6(e) shows a merged image of the two, which clearly proves the presence of both moieties in the larger clusters, indicative of both transferrin species colocalizing to vesicular structures (Fig. 6(e)). However, a zoomed in view of individual clusters (boxes and panels e1 to e4) reveals small but noticeable displacements of the two protein moieties at different positions over the FOV. After optical offset correction (panelsf1-f4) the two species are more clearly colocalized. The data demonstrate both the efficacy of the correction method and the convenience of its application, requiring no fiducial markers in the sample itself and improving the confidence with which biological structures can be interpreted as colocalized at sub-wavelength resolution.

#185209 - $15.00 USD Received 11 Feb 2013; revised 8 Apr 2013; accepted 18 Apr 2013; published 26 Apr 2013

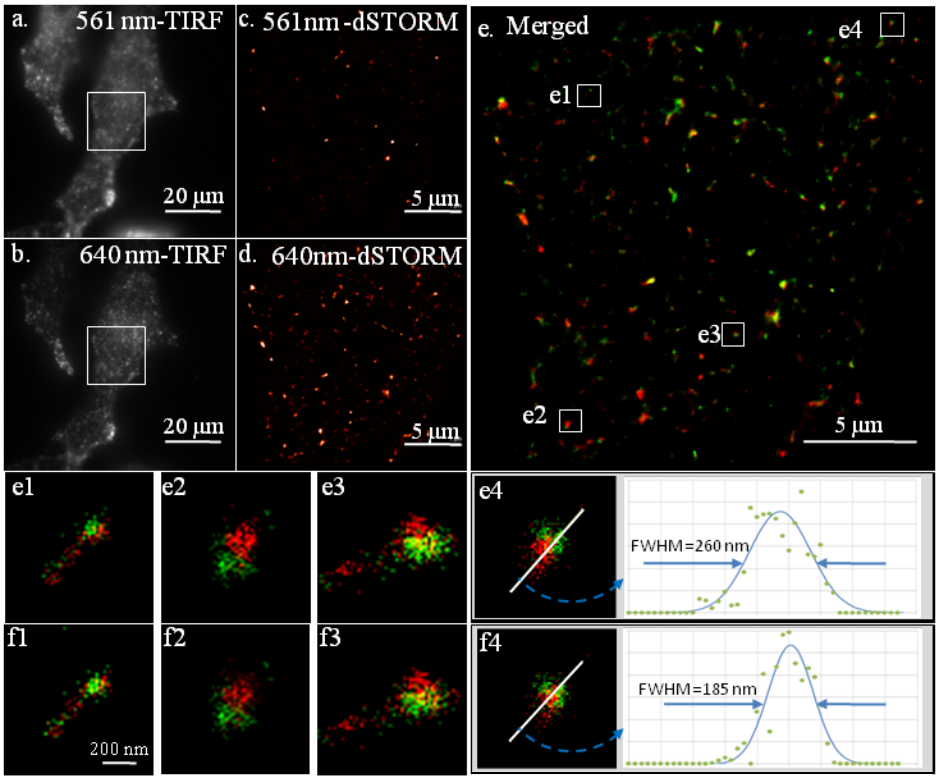

Fig. 6. dSTORM image of double labeled transferrin receptor proteins in HeLa cells using diffraction limited TIRF illumination (a, b), and super-resolved dSTORM imaging (c, d). The merged super-resolved image (e) shows mis-localization between the two images. The depicted four sub-regions before (e1-e4) and after (f1-f4) optical offset correction demonstrate the effectiveness of the correction method. Line-profiles through (e4) and (f4) sub-regions are also depicted.

5. Conclusion

In this paper we present a method to assess chromatic offsets in high NA microscope optics and their effect on multiple color colocalization studies. Chromatic offset causes image distortion on the sub-wavelength scale even for highly corrected microscope optics. We have shown that in the ”sequential” approach the most critical source of mis-registration is the lateral chromatic aberration introduced by the microscope objective. We established the physical basis and not only developed an empirical correction. The distortion is a slowly varying function of optical aperture coordinates and is temporally invariant. We have presented a method for measuring chromatic offsets in practical microscope systems and compared the results with ray-tracing calculations, with good qualitative agreement between the two. Using effective correction algorithms, co-ordinates from different color channels can be effectively mapped onto one another yielding colocalization precisions of the order of one super-resolved pixel or less. If the optical elements in the detection pathway are precisely centered, the colocalization error is small close to the optical axis and a second order polynomial correction is sufficient. In some cases, when the FOV is small, the image distortion may even be neglected. A freely downloadable MATLAB code (rainSTORM) is provided for two-color image registration and for system alignment check [24]. We demonstrated the effectiveness of the method in a biological context through observation of membrane protein clustering and vesicle formation.

#185209 - $15.00 USD Received 11 Feb 2013; revised 8 Apr 2013; accepted 18 Apr 2013; published 26 Apr 2013

Acknowledgment

This research was funded by the Engineering and Physical Sciences Research Council UK (EP/H018301/1), The Alzheimer Research UK Trust (ARUK-EG2012A-1), The Wellcome Trust (089703/Z/09/Z), the Medical Research Council (MR/K015850/1), the Wolfson Foundation, the Chemical and Biological Metrology Program of the UK's National Measurement Office, and by the "TAMOP-4.2.2.C-11/1/KONV-2012-0010" and TAMOP-4.2.2.A-11/1/KONV-2012-0060 projects, supported by the EU and the European Regional Development Fund.

#185209 - $15.00 USD Received 11 Feb 2013; revised 8 Apr 2013; accepted 18 Apr 2013; published 26 Apr 2013